Angewandte Chemie International Edition

Angewandte International Edition Chemie

How to cite: *Angew. Chem. Int. Ed.* **2026**, e9163811
doi.org/10.1002/anie.9163811

RESEARCH ARTICLE

Organic Metal Chalcogenide Films With Giant Birefringence

Zhi-Qing Lan[1,2] | Li-Hua Peng[3,4] | Chao-Hong Xie[1] | Liang-Liang Peng[1] | Shi-Yuan Liu[3,4] | Xiao-Qing Yu[1] | Jiang-Feng Lu[1] | Hong-Gang Gu[3,4] | Guan-E Wang[1] | Gang Xu[1]

[1]State Key Laboratory of Structural Chemistry, Fujian Provincial Key Laboratory of Materials and Techniques toward Hydrogen Energy, Fujian Institute of Research on the Structure of Matter, Chinese Academy of Sciences, Fuzhou, China | [2]University of Chinese Academy of Sciences (UCAS), Beijing, China | [3]School of Mechanical Science and Engineering, Huazhong University of Science and Technology, Wuhan, China | [4]Optics Valley Laboratory, Hubei, China

Correspondence: Hong-Gang Gu (hongganggu@hust.edu.cn) | Guan-E Wang (gewang@fjirsm.ac.cn) | Gang Xu (gxu@fjirsm.ac.cn)

Received: 19 June 2026 | **Revised:** 8 August 2026 | **Accepted:** 20 August 2026

Keywords: birefringence | birefringent film | optical anisotropy | organic metal chalcogenides

ABSTRACT

Birefringent films emerge as a compelling candidate for integrated photonic systems, gracefully balancing superior processability with seamless substrate compatibility. However, birefringent films typically retain only ~20% of bulk crystal performance, which consequently limits film-based birefringence to values rarely exceeding 0.1. To address this limitation, we introduce a two-dimensional van der Waals (2D-vDW) organic metal chalcogenide (OMC) **PbHBT** (HBT = 4-mercaptophenol), featuring "molecular-scale superlattices" of alternating inorganic PbS and organic Ph-OH ligands. **PbHBT** crystal exhibits a birefringence of 0.39@546 nm. A nanoscale thickness-controllable, highly oriented **PbHBT** film was prepared through an economical in situ layer-by-layer (LBL) spin-coating liquid-phase epitaxy (LPE) approach. The birefringence of the **PbHBT** film is 0.3 at 546 nm, maintaining 77% of the birefringence of its bulk crystal. Importantly, the **PbHBT** film achieves a birefringence of 0.65 in the visible spectrum and 0.43 in the near-infrared, which are the highest notes ever achieved by a birefringent film. This excellent birefringence performance stems from the anisotropy of the electron cloud density of different crystal planes of the **PbHBT** and the high consistency of grain orientation after being fabricated into a film. This work opens avenues for thin-film birefringent materials with large intrinsic birefringence and high retention, bridging the bulk-film performance gap.

1 | Introduction

Birefringent materials are essential for polarization control in devices ranging from waveplates to integrated photonic systems [1–10]. The drive towards miniaturization and flexible optoelectronics has created a pressing need to transition from bulk crystals to thin-film formats [11–15]. High-birefringence thin films are key components for on-chip polarizers, waveplates, and polarization beam splitters, which are fundamental building blocks for polarization-division multiplexing in integrated photonics. However, birefringent materials suffer from poor solution processability, and films fabricated from conventional birefringent crystals often introduce random particle orientation and abundant defects, which typically leads to a dramatic reduction in optical anisotropy [16–20]. For instance, the birefringence of TiO_2 drops from 0.306 (bulk crystal) to 0.06 in films; $LiNbO_3$ from 0.08 to 0.048; and MoS_2 from 1.4 to 0.2 [21–27]. In most cases, the birefringence of films remains less than half (often only about

Zhi-Qing Lan and Li-Hua Peng are co-first authors and contributed equally to this work.

20%) of that of bulk crystals. This limitation restricts commercial films to birefringence values rarely exceeding 0.1, posing a critical bottleneck for advanced photonic circuits. Consequently, materials that combine intrinsically high birefringence with facile, high-quality film fabrication are urgently needed.

Two-dimensional van der Waals (2D-vDW) materials, such as metal chalcogenides [28], hexagonal boron nitride (h-BN) [29], exhibit strong structural anisotropy due to the contrast between in-plane covalent bonding and out-of-plane van der Waals interactions, making them promising high-birefringence candidates [30–35]. Among these, organic metal chalcogenides (OMCs) synthesized via coordination chemistry—represent a new class of 2D-vDW materials featuring "molecular-scale superlattices" of alternating inorganic and organic layers [36–38]. Their pronounced in-plane versus out-of-plane structural disparity suggests high optical anisotropy, while their solution-processability offers a clear path to high-quality thin films [39–41]. Despite these attractive attributes, the birefringent properties of OMCs have remained rarely explored to date, leaving their potential for thin-film polarization optics entirely unassessed.

In this work, we investigate, for the first time, the birefringence of an OMC **PbHBT** (HBT = 4-mercaptophenol), which features periodic molecular-scale alternation between inorganic PbS layers and organic Ph-OH ligands. Bulk **PbHBT** crystals exhibit a birefringence of 0.39 at 546 nm. Using layer-by-layer (LBL) liquid-phase epitaxy (LBL-LPE)—enabled by the coordination chemistry of OMCs, we fabricate **PbHBT** films with nanoscale thickness control (~1.3 nm per growth cycle) and high crystallographic orientation. Remarkably, the films (0.3@546 nm) retain 77% of the bulk birefringence, demonstrating that the intrinsic optical anisotropy is largely preserved upon film formation. The **PbHBT** film achieves a birefringence of 0.65 in the visible region and 0.43 in the near-infrared region, surpassing previously reported birefringent films and commercial crystals with birefringence values typical below 0.3. This work opens the door to OMCs as a new class of high-birefringence thin-film materials for polarization optics.

2 | Results and Discussion

Sheet-shaped single crystals of **PbHBT** suitable for single-crystal x-ray diffraction (XRD) were obtained via a solvothermal method (the details are displayed in the Supporting Information). According to the single-crystal XRD data, **PbHBT** crystallizes in non-centrosymmetric monoclinic space group $C2$ (NO.5) with lattice parameters of $a = 7.5546(3)$ Å, $b = 5.1656(2)$ Å, $c = 15.1196(6)$ Å, $\alpha = \gamma = 90.000°$, $\beta = 95.939(4)°$, $Z = 2$, and $V = 586.86(4)$ Å^3 (see detailed crystallographic information listed in Table S1 in the Supporting Information). This space group differs from the centrosymmetric one reported in the literature [42], and the non-centrosymmetric nature of **PbHBT** is further confirmed by nonlinear optical measurements (Figure S1). The crystal structure of **PbHBT** is primarily composed of an alternating stack of PbS inorganic layers and -Ph-OH organic layers. In the PbS inorganic layer, each Pb atom is coordinated by six S atoms, forming a [PbS_6] irregular octahedral structural unit. The bond lengths of Pb-S (2.853(9)–3.257(9) Å) in the PbS_6 octahedron of **PbHBT** are deviation from the ideal octahedron, which indicates that the PbS_6 octahedron shows a slight distortion (Figure 1a). The PbS_6 octahedron is further connected to adjacent ones through two μ_3 shared S atoms, extending along the ab plane to form a two-dimensional {PbS} layer (Figure 1b). In addition, inorganic {PbS} layers covalently anchored by the -Ph-OH organic group through an S-C covalent bond lead to a periodic and ordered arrangement of -Ph-OH organic groups on both side of the inorganic {PbS} layer (Figure 1c). These -Ph-OH-decorated {PbS} layers are further stacked along the crystallographic c-axis via van der Waals interactions between the adjacent organic groups, ultimately affording the overall three-dimensional layered architecture of **PbHBT**. This alternating heterostructure of inorganic PbS layers and aromatic rings underlies the strong anisotropy observed both in-plane and out-of-plane. The powder XRD pattern of the compound is in good agreement with the simulated pattern (Figure 1d), confirming the purity of the product. The presence and uniform distribution of Pb, S, C, and O elements in **PbHBT** single crystal were confirmed by energy dispersive x-ray spectroscopy (EDS) mapping in Figure S2. In addition, the absence of the stretching vibration of -SH at 2560 cm^{-1} in the Fourier transform infrared (FT-IR) spectra (Figure 1e) confirmed the coordination between the metal center and the ligand. The broad bands of 3300 cm^{-1} are assigned to stretching vibrations of O-H. Thermogravimetric analysis curves indicate that **PbHBT** can be stable up to 495 K under a nitrogen atmosphere (Figure S3). To assess air stability, **PbHBT** was exposed to laboratory air for 6 months. XRD patterns recorded showed no significant differences compared to the calculated patterns, confirming excellent air stability (Figure S4). The energy bandgap (E_g) of **PbHBT** was determined to be 1.55 eV from the absorption spectra acquired through reflection measurements, as presented in Figure 1f.

The macroscopic optical anisotropy of **PbHBT** crystals was characterized via a polarizing microscope. The single crystal used for measurement is determined as (001) crystal plane of **PbHBT** by Rigaku FRX diffractometer (Figure S5). As illustrated in Figure 1g, the measurement operates under a cross-polarized geometry where the sample is placed between a polarizer and an orthogonal analyzer. The anisotropic **PbHBT** crystal introduces a phase difference (δ) between the ordinary (o) and extraordinary (e) eigenmodes, resulting in birefringence-induced interference colors that map the retardance distribution. Azimuthal-dependent transmission confirms the high quality of the single crystal. As the sample is rotated, the transmitted intensity (I) follows the theoretical dependence $I \propto \sin^2(2\varphi)\sin^2(\delta/2)$, where φ is the rotation angle. Consequently, the crystal displays distinct extinction states at $\varphi = 0°$ and 90° (where eigenmodes align with the polarizer axis) and maximum transmittance at $\varphi = 45°$ (Figures 1h and S6). This four-fold symmetry of extinction and brightening per full rotation confirms the single-crystalline nature and uniform orientation of the domain. Notably, at the 45° diagonal position, the crystal exhibits a uniform vivid reddish-magenta color. According to the standard Michel-Levy interference color chart, this specific hue is identified as the first-order red, qualitatively indicating a retardation (Γ) of approximately 550 nm. This visual estimation agrees remarkably well with the quantitative measurement using a Berek compensator, where a retardation of $\Gamma = 550$ nm was precisely determined for the $d =$ 1.4-μm-thick sample at 546 nm (Figure S7a). The resulting bire-

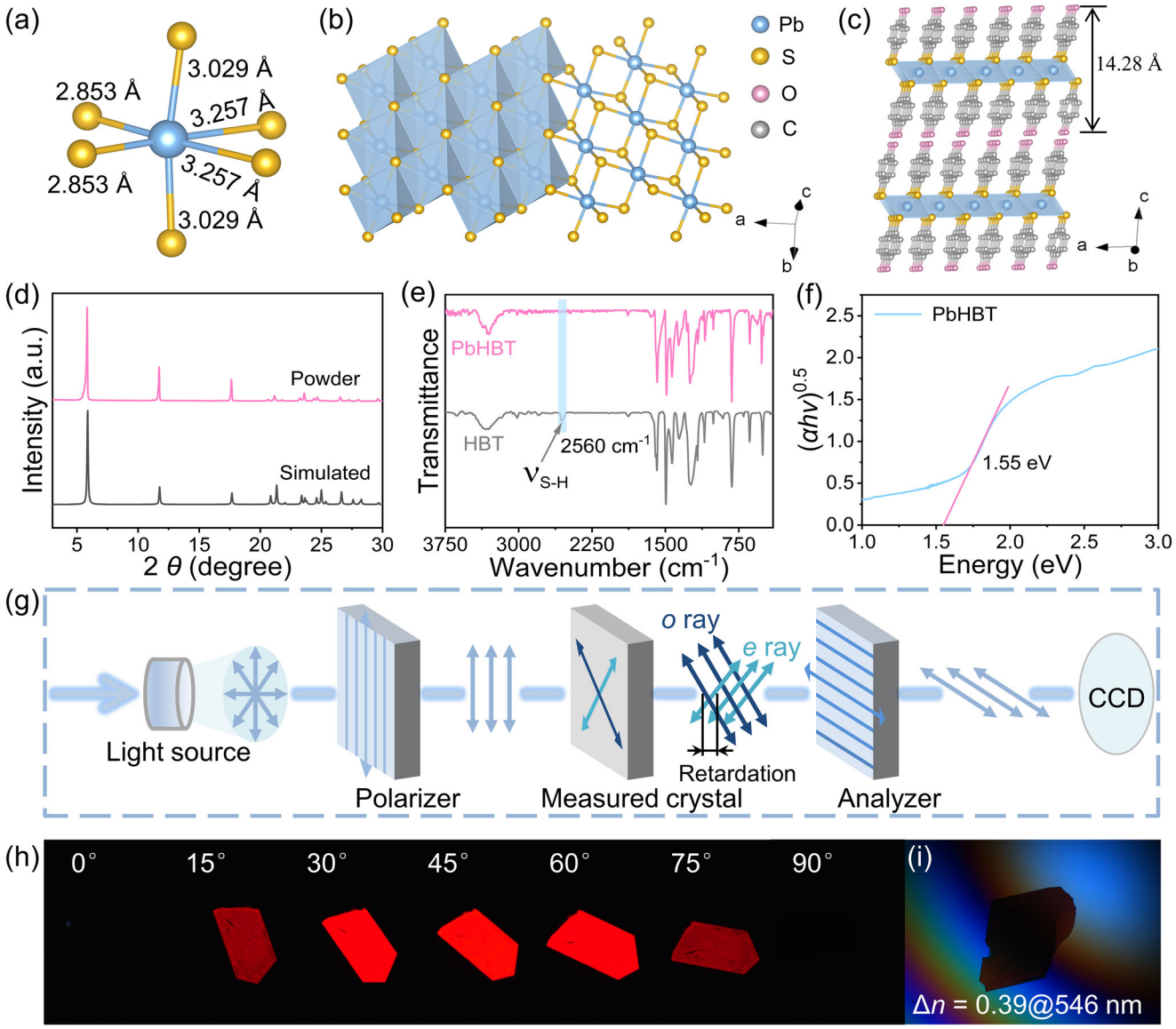

FIGURE 1 | (a) The structural unit of [PbS_6] octahedra. (b) The inorganic layer. (c) The packing structure of PbHBT. (d) PXRD patterns. (e) FT-IR spectra of PbHBT nanosheets. (f) UV-Vis diffuse reflection spectra of PbHBT. (g) Schematic diagram of polarizing microscope. (h) Optical images of PbHBT crystal irradiated by orthogonally polarized light at different rotation angles. (i) The PbHBT crystal observed at complete extinction with a Berek compensator.

fringence of $\Delta n = \Gamma/d \approx 0.39$ further underscores the exceptional optical anisotropy inherent to the **PbHBT** structure (Figures 1i and S7).

Translating the intrinsic bulk birefringence crystal into a functional film form presents a critical challenge for device integration. LBL-LPE demonstrates distinct advantages in growing oriented films due to its unique growth mechanism [43–45]. The near-equilibrium growth environment enables precise lattice matching and crystallographic alignment on the substrate, resulting in highly oriented epitaxial layers with well-defined in-plane and out-of-plane orientations. This technique facilitates the formation of films with exceptional crystalline perfection, minimal interfacial defects, and controlled morphological characteristics. We adopt an in situ LBL spin-coating LPE method to prepare uniformly oriented **PbHBT** film. First, the substrate was spun with the solution containing Pb^{2+}, which was then followed by spinning of HBT to chelate with Pb^{2+}, thereby achieving the first growth cycle (Figure 2a). This cycle of operation was meticulously repeated to facilitate the epitaxial growth of **PbHBT-xC** films by this controlled LBL-LPE sequence (details see Supporting Information). It is noteworthy that the dimensions of the **PbHBT** film can reach the centimeter scale (Figure S8). Due to the flexibility of the polydimethylsiloxane (PDMS) substrate, the film could be repeatedly bent and relaxed at least 50 times without any visible cracks (Figure S9). Scanning electron microscopy (SEM) analysis indicates that the growth of **PbHBT** progresses through distinct stages. **PbHBT** initially nucleates as discrete island-like nanosheets during the early growth phase. As deposition proceeds, these isolated islands undergo lateral expansion and densification, ultimately leading to the formation of a fully coalesced, continuous film with high structural uniformity on glass (Figure 2b). Atomic force microscopy (AFM) characterization of the **PbHBT** films indicates a thickness increment

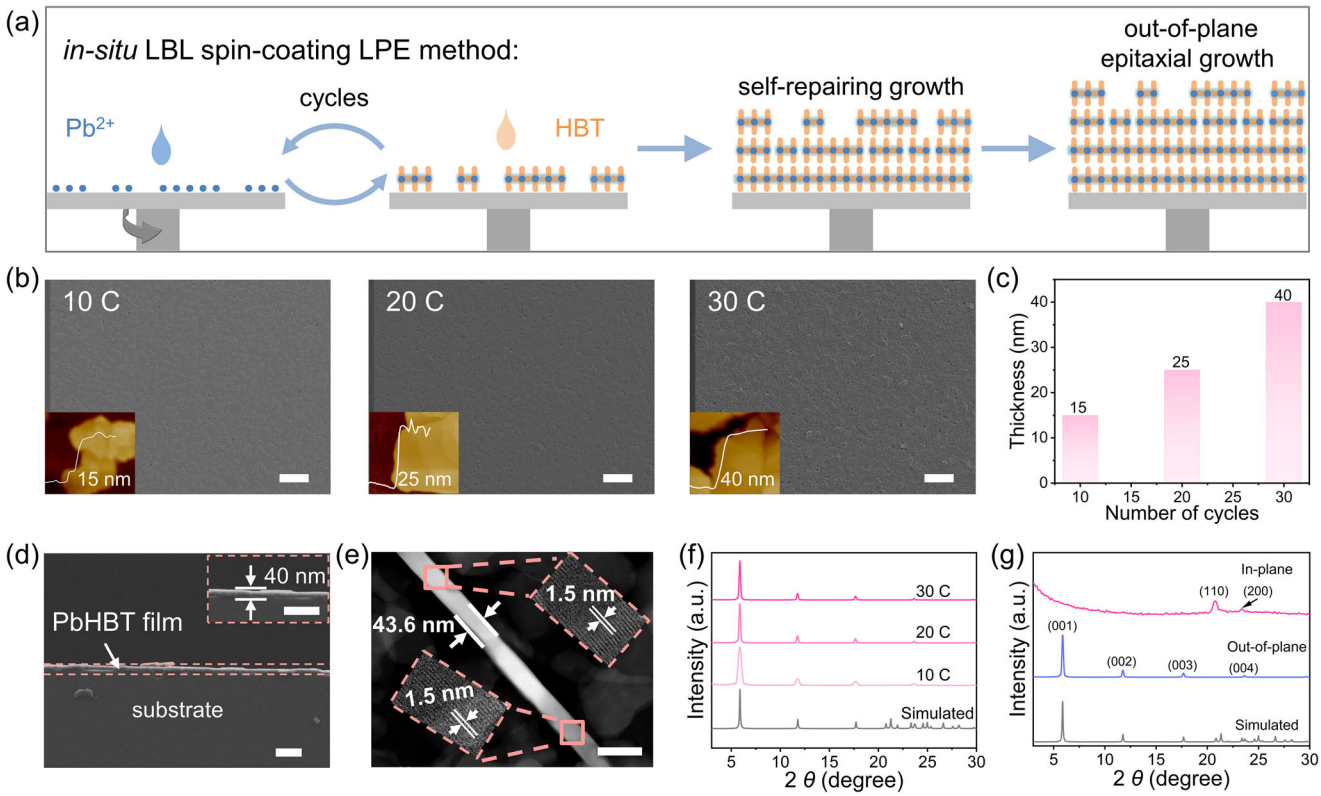

FIGURE 2 | (a) Schematic illustration of in situ LBL spin-coating LPE method of PbHBT film. (b) SEM of PbHBT-xC ($x = 10, 20, 30$) films based on in situ LBL spin-coating LPE method, scale bar: 2 μm. Insets are AFM images of PbHBT-xC films. (c) Growth cycles-dependent thickness of PbHBT-xC films. (d) SEM cross-sectional view of PbHBT-30C film, scale bar: 500 nm. Inset is magnification image. (e) Cross-sectional HAADF-STEM of PbHBT-30C film (scale bar: 100 nm). Insets are HR-TEM images. (f) XRD of PbHBT-xC ($x = 10, 20, 30$) films. (g) In-plane and out-of-plane XRD of PbHBT film with a thickness of 40 nm.

of approximately 1.3 nm per growth cycle (Figure 2c). Cross-sectional SEM imaging reveals a continuous, uniform film with a thickness of 40 nm for **PbHBT-30C** (Figure 2d). The cross-sectional high-angle annular dark-field scanning transmission electron microscopy (HAADF-STEM) image shows the side view of the film with a thickness of ~43.6 nm for the **PbHBT-30C** film, which is consistent with SEM data (Figure 2e). Notably, the cross-sectional high-resolution transmission electron microscopy (HRTEM) exhibits well-ordered lattice fringes throughout the film, confirming its highly oriented crystalline texture. The measured interplanar spacing is 1.5 nm, which corresponds to the (001) planes, indicating an epitaxial nature with out-of-plane orientation. HAADF-STEM elemental mapping images (Figure S10) further verify the elemental composition of Pb, S, and O, which is consistent with that of the crystal. The selected area electron diffraction (SAED) pattern (Figure S11) acquired from the in-plane region of the films shows bright and distinct spots, which can be assigned to the indices of (hk0) face of the **PbHBT** film, verifying the high crystallinity and well-aligned out-of-plane orientation of the films. We propose that the growth of **PbHBT** films may occur via a unique mode characterized by "self-limited in-plane and epitaxial out-of-plane" growth mode. The in-plane growth (parallel to the substrate) shows self-limiting behavior, while the out-of-plane growth (perpendicular to the substrate) follows an epitaxial mechanism. This distinctive growth mode, together with the observed microstructural characteristics, collectively governs the final performance of the film and provides a structural basis for understanding its high birefringence properties.

The XRD patterns reveal that the intensity of the XRD peaks for the **PbHBT-xC** films increases progressively with the addition of layers (Figure 2f). It is worth noting that the diffraction peaks become progressively narrower as the number of deposition cycles increases, which, according to the Scherrer equation, reflects an increase in the out-of-plane crystalline coherence length (Table S2). The in-plane and out-of-plane XRD patterns of the **PbHBT-30C** film with a thickness of 40 nm are shown in Figure 2g. The peaks in the out-of-plane pattern are exclusively indexed to the (00l) reflections, while the corresponding peaks in the in-plane pattern are absent. The out-of-plane XRD data of the **PbHBT** film exhibit sharp peaks at 5.88°, 11.76°, 17.65°, and 23.63°, which correspond to the (001), (002), (003), and (004) diffraction peaks of simulated bulk **PbHBT**, demonstrating highly oriented growth of the **PbHBT** film along the (001) orientation. The in-plane grazing-incidence x-ray diffraction (GIXRD) pattern shows pronounced diffraction peaks at 20.75° and 23.39°, indexed to the (110) and (200) planes, respectively. These findings further confirm that the **PbHBT** film undergoes epitaxial growth with *c*-axis orientation. The preferential crystallographic orientation of **PbHBT** film was further characterized by grazing-incidence wide-angle x-ray scattering (GIWAXS), as shown in Figure S12. High-order diffraction (00L) reflection spots at q_z indicate the highly oriented nature of the film.

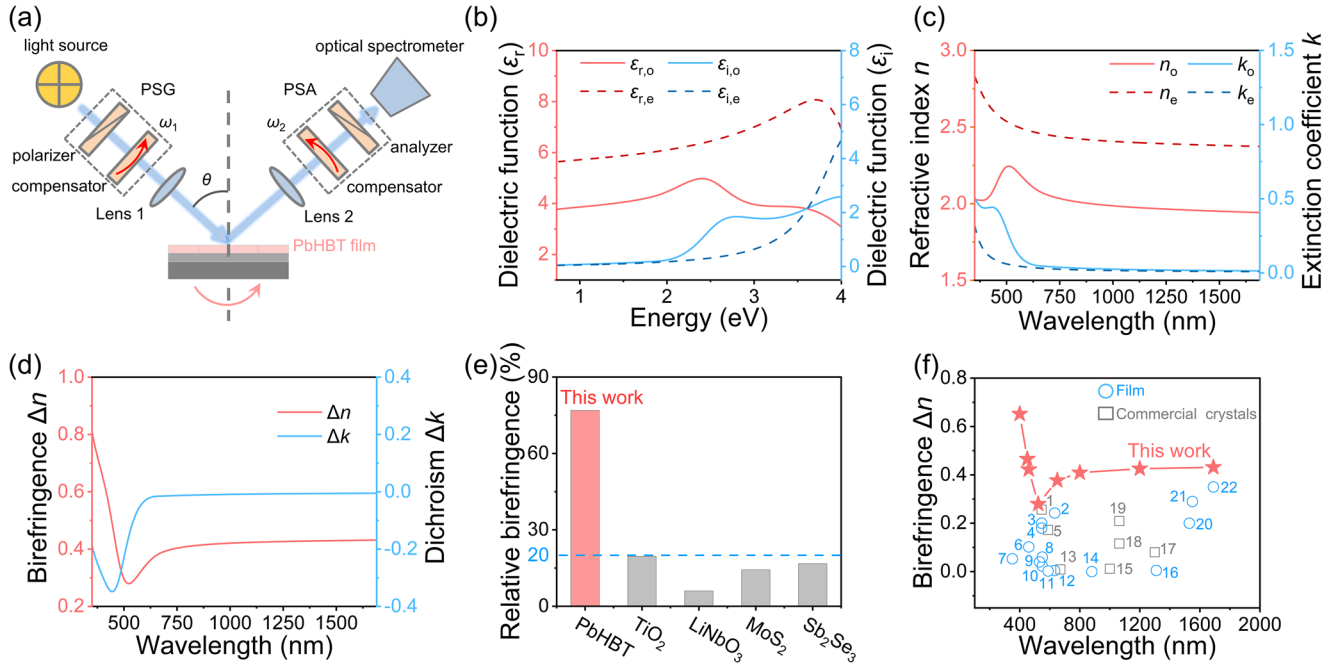

FIGURE 3 | Dielectric and optical anisotropy of the PbHBT-20C film, thicknesses 25 nm. (a) The working principle of Mueller matrix spectroscopic ellipsometer. θ represents the incident angle. The Mueller matrix is obtained by dual-rotating compensators. (b) The real part of the dielectric functions and the imaginary part of the dielectric tensor of PbHBT film in ordinary and extraordinary directions. (c) The experimental refractive indices and extinction coefficients of the PbHBT film in ordinary and extra-ordinary directions. (d) The experimental birefringence and dichroism of PbHBT film. (e) The degree of birefringence retained by the film compared to that of the crystal. (f) Comparison of the birefringence of PbHBT film with different birefringent films (including 2: BPDA-PDA [46], 3: ITO [47], 4: GO [17], 6: CAS-10 [20], 7: Al_2O_3 [48], 8: TiO_2 [22], 9: PPQ [49], 10: SiO_2 [50], 11: (PVA)-based QWP [51], 12: MO/PVA [52], 14: Plasmonic chiral polymer [53], 17: $LiNbO_3$ [24], 20: MoS_2 [27], 21: Sb_2Se_3 [16], and 22: carbon nanotubes film [19]) and commercial birefringent crystals (including 1: TiO_2 [21], 5: calcite [54], 13: quartz [54], 15: MgF_2 [55], 16: $LiNbO_3$ [25], 18: α-BaB_2O_4 [56], and 19: YVO_4 crystal [57]).

To quantitatively characterize the optical anisotropy, the complete dielectric tensor of the **PbHBT** film was determined using Mueller matrix spectroscopic ellipsometry [58] (Figure 3a). Full Muller matrix spectrum was acquired at variable angles of incidence (AOI) from 50° to 70° to enhance sensitivity. The optical response of the **PbHBT** film was described by constructing a biaxial anisotropic film model based on the Berreman 4 × 4 matrix method [59], in which the dielectric tensor can be simply described by two diagonal components, namely the dielectric functions along with the ordinary direction (i.e., the in-plane direction) and extra-ordinary direction (the out-of-plane direction). The complex dielectric tensor can be determined from the measured Mueller matrix spectra based on the constructed optical model for **PbHBT** film. To physically describe the dispersion, the dielectric functions were parameterized using a combination of Tauc–Lorentz, Lorentz, and Gaussian oscillators. This hybrid oscillator model strictly enforces Kramers–Kronig consistency, thereby ensuring the physical validity of the extracted parameters. Furthermore, to guarantee the uniqueness of the mathematical solution and decouple the correlation between film thickness and dielectric functions, a global fitting procedure was performed simultaneously across all measured AOIs. The reliability of the fit was confirmed by a minimized mean squared error (MSE), indicating excellent agreement between the experimental spectra and the theoretical anisotropic model (Figure S13).

The extracted dielectric functions of the **PbHBT-20C** film are presented in Figure 3b across the wavelength range of 350–1690 nm. The diagonal components of the dielectric tensor reveal distinct anisotropy in both the real (ε_r) and imaginary (ε_i) parts between the ordinary and extra-ordinary directions. Consequently, the anisotropic refractive indices (n_o, n_e) and extinction coefficients (k_o, k_e) were extracted over the measured spectral range (Figure 3c). Importantly, the birefringence of the **PbHBT** film (0.30@546 nm) is modestly reduced relative to the bulk single crystal (0.39@546 nm) (Figure 3d), it strikingly maintains about 77% of the anisotropic optical of single crystal. This level of property retention is exceptional among birefringent films and marks a significant advancement over materials such as TiO_2 (0.306 for bulk crystal, 0.06 for film), $LiNbO_3$ (0.08 for bulk crystal, 0.048 for film) and so on (Table S3), which undergo substantial birefringence loss in film configurations (Figure 3e). Remarkably, the **PbHBT** film exhibits a giant birefringence, peaking at $\Delta n \approx 0.65$ in the visible region and maintaining a substantial value of $\Delta n \approx 0.43$ extending into the near-infrared spectrum (Figure 3d, Table S4). As the wavelength increases, the birefringence of **PbHBT** film remains relatively stable 0.43 at near-infrared wavelengths. Repeated measurements on different batches show good consistency in the birefringence values (Figure S14). To the best of our knowledge, these values significantly surpass those of state-of-the-art birefringent films and exceed common commercial crystals, including calcite [54], quartz [54], MgF_2 [55], α-BaB_2O_4 [56], and YVO_4 [57] (Figure 3f). Additionally, the linear dichroism (Δk) approaches zero in the infrared region, which is a critical attribute for low-loss polarization modulation devices, such as waveplates. These experimental results show

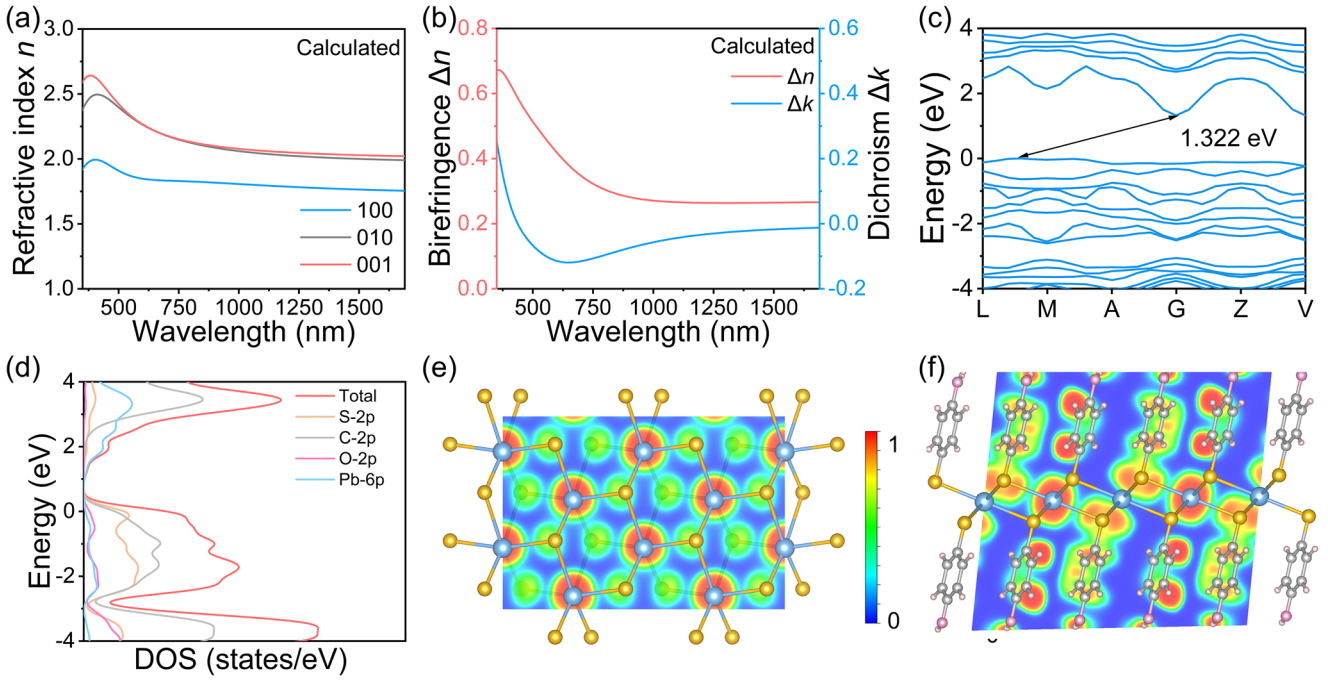

FIGURE 4 | (a) The refractive index of PbHBT along 100, 010, and 001 direction based on the first-principles calculations (001 represents the out-of-plane direction; 100&010 represent the in-plane directions). (b) Birefringence and dichroism of PbHBT calculated by the first-principles. (c) Electronic band structure and (d) partial density of states (PDOS) for PbHBT obtained from theoretical calculations. (e) Slice cutting through Pb atoms along (001) crystal plane parallel to PbS layers. (f) Slice cutting through Pb atoms along (010) crystal plane perpendicular to PbS layers. Iso-value increases from blue to red, and the maximum ELF value is scaled to 1. (Blue, yellow, gray, pink and light pink balls represent Pb, S, C, O, and H atoms, respectively.).

excellent agreement with first-principles calculations (Figures 4a and S15). As revealed by the computational results, the refractive index dispersion curves in Figure 4a exhibit clear anisotropy. The birefringence of **PbHBT** film in the visible region was calculated to be 0.64, which is in agreement with the experimental value (0.65). As the wavelength increases, the birefringence tends to be stable above 900 nm (Figure 4b).

In order to demystify the underlying relationship between the structure and optical performance of **PbHBT** film, we perform first-principles calculations based on the plane-wave pseudopotential method implemented in the Cambridge Serial Total Energy Package (CASTEP) package. Density functional theory (DFT) calculations (details in Supporting Information) revealed that **PbHBT** exhibited an indirect band gap (Figure 4c). The electronic band structure calculation by the Generalized Gradient Approximation (GGA) functional with the Perdew-Burke-Ernzerh (PBE) function shows that the band gap of **PbHBT** is 1.32. This calculated value agrees well with the experimental result. Figure 4d shows the density of states (DOS) and partial DOS on the constituent atoms of **PbHBT**. The top of the valence bands (VB) is predominantly composed of S 2p, C 2p, and O 2p orbitals, while the bottom of the conduction bands (CB) is primarily occupied by Pb 6p and S 2p orbitals. The optical properties of **PbHBT** are determined by electronic states near the band gap, with the -Ph-OH motifs and PbS inorganic layer identified as the key structural features governing these characteristics.

The depictions of the highest occupied molecular orbitals (HOMO) and lowest unoccupied molecular orbitals (LUMO) for **PbHBT** provide a clear illustration of how each functional unit contributes to optical anisotropy (Figure S16). The HOMO involves a combination of S 2p, C 2p and O 2p, and π-conjugated orbitals. The LUMO involve a combination of Pb 6p and S 2p. The HOMO and LUMO diagrams of **PbHBT** clearly demonstrates significant anisotropy in electron density. This observation leads to the conclusion that the periodic arrangement of organic motifs and PbS layer, plays a crucial role in generating the pronounced optical anisotropy observed in **PbHBT**. In addition, we further reveal the mechanism of giant optical anisotropy from the microscopic point of view. We further analyzed the electron localization function (ELF) maps [60] projected on crystal planes parallel to and perpendicular to PbS layers for **PbHBT** (Figure 4e,f). The electron cloud of the PbS octahedra can be seen directly in the (001) plane, and the electron cloud around the -Ph-OH motifs is strongly optically anisotropic. It can be intuitively seen that the electron cloud density exhibits significant difference in different crystal planes, resulting in strong optical anisotropy in **PbHBT**.

The in situ LBL spin-coating LPE method is not limited to **PbHBT** but can be extended to other structurally related organic metal chalcogenide complexes. As a demonstration, another OMC, $Pb(MSBT)_2$ (MSBT = 4-(methylthio)benzenethiol) [42], was selected for preliminary investigation (Figure S17). The refractive index dispersion curves calculated for this material reveal clear optical anisotropy in the near-infrared region, with a theoretical birefringence of approximately 0.4 (Figure S18). To validate this prediction, $Pb(MSBT)_2$ films were prepared on glass substrates using the same in situ LBL spin-coating LPE method. The out-of-plane (00L) and in-plane (hk0) XRD

patterns exhibit well-defined diffraction peaks, confirming the epitaxial growth along c-axis (Figure S19a). The resulting films also display a sheet-like surface morphology, as shown in Figure S19b. Mueller matrix spectroscopic ellipsometry measurements yield a birefringence of $\Delta n = 0.3$ in the near-infrared spectrum (Figure S20), which is slightly lower than the theoretical value of 0.4 but still retains approximately 75% of the predicted anisotropy.

3 | Conclusion

In summary, we have demonstrated that OMCs, a class of 2D-vDW materials synthesized via coordination chemistry, offering a previously unexplored platform for high-performance thin-film birefringence. By constructing **PbHBT**, we show that the periodic molecular-scale superlattice of inorganic and organic layers gives rise to strong anisotropic electron distribution, yielding a bulk birefringence of 0.39 at 546 nm. More importantly, the solution-processable nature of OMCs enables the fabrication of highly oriented, crystalline films (0.3@546 nm) via LBL-LPE, which retains 77% of the bulk birefringence-substantially outperforming conventional birefringent films that typically preserve less than half of their bulk values. The resulting **PbHBT** films achieve a birefringence of 0.65 in the visible and 0.43 in the near-infrared, surpassing both existing film-based and commercial crystalline birefringent materials. Beyond demonstrating a record-performance material, this work establishes OMCs as a general, molecularly designable family for polarization optics, where the inorganic backbone provides structural anisotropy and the organic ligands offer synthetic tunability and solution processability. We anticipate that this synergy between coordination chemistry and LBL assembly will open new avenues for integrating high-birefringence thin films into next-generation photonic circuits, flexible optoelectronics, and on-chip polarization control devices.

Author Contributions

G.X., G.W. and H.G. contributed to the conception of the research and revise the manuscript. H.G. provided suggestions for research. H.G. and S.L. guided the Mueller matrix spectroscopic ellipsometry analyses. L.P. performed the Mueller matrix spectroscopic ellipsometry measurement. Z.L. performed the experiments and wrote the manuscript. L.P., C.X., X.Y. and J.L. assisted in the experimental and theoretical analysis. All authors discussed the results and reviewed the manuscript.

Acknowledgements

This work was financially supported by the National Natural Science Foundation of China (22271281, 22422508, 22325109, 62227815, 22494633, 22505265, 22405274, 52450258, and 52575624), Self-deployment Project Research Program of Haixi Institutes, Chinese Academy of Sciences (CXZX-2023-GS03), the Strategic Priority Research Program of the Chinese Academy of Sciences, Grant No. (XDB1170000), and the Key Research Project of Chinese Academy of Sciences under Grant (KGFZD-145-25-21).

Conflicts of Interest

The authors declare no conflicts of interest.

Data Availability Statement

The data that support the findings of this study are available from the corresponding author upon reasonable request.

References

1. W. Ma, P. Alonso-González, S. Li, et al., "In-Plane Anisotropic and Ultra-Low-Loss Polaritons in a Natural van der Waals Crystal," *Nature* 562 (2018): 557–562, https://doi.org/10.1038/s41586-018-0618-9.

2. W. Ma, G. Hu, D. Hu, et al., "Ghost Hyperbolic Surface Polaritons in Bulk Anisotropic Crystals," *Nature* 596 (2021): 362–366, https://doi.org/10.1038/s41586-021-03755-1.

3. S. Niu, G. Joe, H. Zhao, et al., "Giant Optical Anisotropy in a Quasi-One-Dimensional Crystal," *Nature Photonics* 12 (2018): 392–396, https://doi.org/10.1038/s41566-018-0189-1.

4. Y. Sun, Y. Li, X. Song, S. Zhao, T. Zhou, and J. Zhang, "A Robust Phosphonate-Based Hydrogen-Bonded Organic Framework Birefringent Crystal," *Advanced Functional Materials* 35 (2025): 2413107, https://doi.org/10.1002/adfm.202413107.

5. X. Chen, B. Zhang, F. Zhang, et al., "Designing an Excellent Deep-Ultraviolet Birefringent Material for Light Polarization," *Journal of the American Chemical Society* 140 (2018): 16311–16319, https://doi.org/10.1021/jacs.8b10009.

6. Q. Ren, C. Cui, X. Chen, et al., "$[Hg_3Se_2]_2$-Cluster Drives Giant Optical Anisotropy and Broad Infrared Transparency," *Nature Communications* 17 (2026): 40, https://doi.org/10.1038/s41467-025-66148-2.

7. Y. Du, W. Che, Y. Shi, et al., "$[HgX_2]$ Linear Group Enabled Ultraviolet Birefringent Crystal $RbHg_5Br_{11}$ With Strong Optical Anisotropy and Wide Bandgap," *Advancement of Science* 12 (2025): e14304, https://doi.org/10.1002/advs.202514304.

8. J. Guo, A. Tudi, S. Han, Z. Yang, and S. Pan, "α-SnF 2: A UV Birefringent Material With Large Birefringence and Easy Crystal Growth," *Angewandte Chemie International Edition* 2 (2021): 3540–3544, https://doi.org/10.1002/anie.202014279.

9. Z. Sun, B. Wu, X. Wang, et al., "Enhancing Birefringence and Second-Harmonic Generation Response via Aliovalent Metal Substitution," *Chinese Journal of Structural Chemistry* 45 (2026): 100790.

10. Z. Bai, S. Zhao, K. M. Ok, and J. Luo, "Organic π-Conjugated Units as Versatile Building Blocks for High-Performance Birefringent Crystals," *Chinese Journal of Structural Chemistry* 45 (2026): 100802.

11. A. Tudi, S. Han, Z. Yang, and S. Pan, "Potential Optical Functional Crystals With Large Birefringence: Recent Advances and Future Prospects," *Coordination Chemistry Reviews* 459 (2022): 214380, https://doi.org/10.1016/j.ccr.2021.214380.

12. Y. Zhou, Z. Guo, H. Gu, et al., "A Solution-Processable Natural Crystal With Giant Optical Anisotropy for Efficient Manipulation of Light Polarization," *Nature Photonics* 18 (2024): 922–927, https://doi.org/10.1038/s41566-024-01461-8.

13. L. Zhang, Z. Wu, J. Yan, et al., "Enhancement of Birefringence in Alkali Metal Sulfates Induced by Rare Earth Metal-Centered Polyhedra and Structure Regulation via Cations," *Chemistry of Materials* 37 (2025): 8996–9003, https://doi.org/10.1021/acs.chemmater.5c02373.

14. P. Guo, X. Zhang, Y. Guo, et al., "Giant Birefringence and Solar-Blind Ultraviolet Transmission by Coordination-Induced Assembly of π-Conjugated Pyridine–Carboxylate," *Angewandte Chemie International Edition* 64 (2025): e202508997.

15. C. Jin, Y. Li, C.-A. Chen, et al., "Sulfonated Module Aggregation for Ultrahigh Birefringence in Aqueous-Processable Crystals," *Journal of the American Chemical Society* 147 (2025): 39964–39973, https://doi.org/10.1021/jacs.5c15741.

16. L. G. Greca, J. Lehtonen, B. L. Tardy, J. Guo, and O. J. Rojas, "Heteroepitaxial Growth of Highly Anisotropic Sb_2Se_3 Films on GaAs," *Mater* 5 (2018): 408–415.

17. T. Zou, B. Zhao, W. Xin, et al., "Birefringent Response of Graphene Oxide Film Structurized via Femtosecond Laser," *Nano Research* 15 (2022): 4490–4499, https://doi.org/10.1007/s12274-021-3505-x.

18. D. Hu, K. Chen, X. Chen, X. Guo, M. Liu, and Q. Dai, "Tunable Modal Birefringence in a Low-Loss Van Der Waals Waveguide," *Advanced Materials* 31 (2019): 1807788, https://doi.org/10.1002/adma.201807788.

19. J. Lynch, E. Smith, A. Alfieri, et al., "Gate-Tunable Optical Anisotropy in Wafer-Scale, Aligned Carbon Nanotube Films," *Nature Photonics* 18 (2024): 1176–1184, https://doi.org/10.1038/s41566-024-01504-0.

20. J. Ding, L. Huang, L. Chang, Z. Gu, and J. Zhang, "Homochiral Birefringence Hydrogen-Bonded Organic Framework Films for Highly Circularly Polarized Luminescence," *Angewandte Chemie International Edition* 65 (2026): e4678241.

21. W. M. Sinton, "Birefringence of Rutile in the Infrared," *Journal of the Optical Society of America A* 51 (1961): 1309_1–1310, https://doi.org/10.1364/JOSA.51.1309_1.

22. H. Miyata, H. Suzuki, Y. Sugahara, K. Zhang, T. Asahi, and Y. Yamauchi, "Full-Multiscale Spontaneous Organization for Optically Anisotropic Titania Films," *Small* 21 (2025): 2501782, https://doi.org/10.1002/smll.202501782.

23. H. Miyata, Y. Fukushima, K. Okamoto, et al., "Remarkable Birefringence in a TiO_2–SiO_2 Composite Film With an Aligned Mesoporous Structure," *JACS* 133 (2011): 13539–13544.

24. B. Wang, T. Zhu, Y. Liu, H. Yang, R. Pan, and J. Li, "Chiral Resonant Modes Induced by Intrinsic Birefringence in Lithium Niobate Metasurfaces," *Physical Review Letter* 134 (2025): 113802, https://doi.org/10.1103/PhysRevLett.134.113802.

25. D. E. Zelmon, D. L. Small, and D. Jundt, "Infrared Corrected Sellmeier Coefficients for Congruently Grown Lithium Niobate and 5 Mol% Magnesium Oxide–Doped Lithium Niobate," *Journal of the Optical Society of America B* 14 (1997): 3319.

26. D. Hu, X. Yang, C. Li, et al., "Probing Optical Anisotropy of Nanometer-Thin van der Waals Microcrystals by Near-Field Imaging," *Nature Communications* 8 (2017): 1471, https://doi.org/10.1038/s41467-017-01580-7.

27. K. M. Islam, R. Synowicki, T. Ismael, I. Oguntoye, N. Grinalds, and M. D. Escarra, "In-Plane and Out-of-Plane Optical Properties of Monolayer," *Advanced Photonics Research* 2 (2021): 2000180.

28. G. A. Ermolaev, D. V. Grudinin, Y. V. Stebunov, et al., "Giant Optical Anisotropy in Transition Metal Dichalcogenides for Next-Generation Photonics," *Nature Communications* 12 (2021): 854.

29. A. Segura, L. Artús, R. Cuscó, T. Taniguchi, G. Cassabois, and B. Gil, "Natural Optical Anisotropy of h-BN: Highest Giant Birefringence in a Bulk Crystal through the Mid-Infrared to Ultraviolet Range," *Physical Reviews Materials* 2 (2018): 024001, https://doi.org/10.1103/PhysRevMaterials.2.024001.

30. N. Mao, J. Tang, L. Xie, et al., "Optical Anisotropy of Black Phosphorus in the Visible Regime," *Journal of the American Chemical Society* 138 (2016): 300–305, https://doi.org/10.1021/jacs.5b10685.

31. M. Schubert, T. Hofmann, C. M. Herzinger, and W. Dollase, "Generalized Ellipsometry for Orthorhombic, Absorbing Materials: Dielectric Functions, Phonon Modes and Band-to-band Transitions of Sb_2S_3," *Thin Solid Films* 455–456 (2004): 619–623, https://doi.org/10.1016/j.tsf.2003.11.207.

32. Q. Guo, Q. Zhang, T. Zhang, et al., "Colossal In-plane Optical Anisotropy in a Two-Dimensional van der Waals Crystal," *Nature Photonics* 18 (2024): 1170–1175, https://doi.org/10.1038/s41566-024-01501-3.

33. H. Yang, H. Jussila, A. Autere, et al., "Optical Waveplates Based on Birefringence of Anisotropic Two-Dimensional Layered Materials," *ACS Photonics* 4 (2017): 3023–3030, https://doi.org/10.1021/acsphotonics.7b00507.

34. Y. Y. Wang, J. D. Zhou, J. Jiang, et al., "In-Plane Optical Anisotropy in ReS_2 Flakes Determined by Angle-Resolved Polarized Optical Contrast Spectroscopy," *Nanoscale* 11 (2019): 20199–20205, https://doi.org/10.1039/C9NR07502J.

35. H. Wang, J. Liu, M. Li, et al., "A New 2D van der Waals Material With Air Stability and In-Plane Anisotropy," *Chinese Journal of Structural Chemistry* 42 (2023): 100099.

36. G. Wang, S. Luo, T. Di, Z. Fu, and G. Xu, "Layered Organic Metal Chalcogenides (OMCs): From Bulk to Two-Dimensional Materials," *Angewandte Chemie International Edition* 61 (2022): e202203151, https://doi.org/10.1002/anie.202203151.

37. Y. Wen, G. Wang, X. Jiang, X. Ye, W. Li, and G. Xu, "A Covalent Organic–Inorganic Hybrid Superlattice Covered With Organic Functional Groups for Highly Sensitive and Selective Gas Sensing," *Angewandte chemie* 60 (2021): 19710–19714.

38. B. Choi, K. Jo, M. Rahaman, et al., "Giant Optical Anisotropy in 2D Metal–Organic Chalcogenates," *ACS Nano* 18 (2024): 25489–25498, https://doi.org/10.1021/acsnano.4c05043.

39. B. Trang, M. Yeung, D. C. Popple, et al., "Tarnishing Silver Metal Into Mithrene," *Journal of the American Chemical Society* 140 (2018): 13892–13903, https://doi.org/10.1021/jacs.8b08878.

40. A. Giri, G. Park, H. Yang, M. Pal, J. Kwak, and U. Jeong, "Synthesis of 2D Metal Chalcogenide Thin Films through the Process Involving Solution–Phase Deposition," *Advanced Materials* 30 (2018): 1707577.

41. L. Maserati, S. Pecorario, M. Prato, and M. Caironi, "Understanding the Synthetic Pathway to Large-Area, High-Quality [AgSePh] ∞ Nanocrystal Films," *Journal of Physical Chemistry C* 124 (2020): 22845–22852, https://doi.org/10.1021/acs.jpcc.0c07330.

42. H. Yang, S. Mandal, Y. H. Lee, et al., "Dimensionality Engineering of Lead Organic Chalcogenide Semiconductors," *Journal of the American Chemical Society* 145 (2023): 23963–23971, https://doi.org/10.1021/jacs.3c05745.

43. J. Zhuang, D. Ceglarek, S. Pethuraj, and A. Terfort, "Rapid Room-Temperature Synthesis of Metal–Organic Framework HKUST-1 Crystals in Bulk and as Oriented and Patterned Thin Films," *Advanced Functional Materials* 21 (2011): 1442–1447, https://doi.org/10.1002/adfm.201002529.

44. R. Zheng, Z. Fu, W. Deng, et al., "The Growth Mechanism of a Conductive MOF Thin Film in Spray-Based Layer-by-Layer Liquid Phase Epitaxy," *Angewandte Chemie International Edition* 61 (2022): e202212797, https://doi.org/10.1002/anie.202212797.

45. Z.-G. Gu and J. Zhang, "Epitaxial Growth and Applications of Oriented Metal–Organic Framework Thin Films," *Coordination Chemistry Reviews* 378 (2019): 513–532, https://doi.org/10.1016/j.ccr.2017.09.028.

46. J. Diao and D. W. Hess, "Through-Plane Uniformity of Optical Anisotropy in Spin-Coated Biphenyl Dianhydride-p-Phenylenediamine Films," *Thin Solid Films* 483 (2005): 226–231, https://doi.org/10.1016/j.tsf.2004.11.246.

47. A. Cerkauskaite, R. Drevinskas, A. Solodar, I. Abdulhalim, and P. G. Kazansky, "Form-Birefringence in ITO Thin Films Engineered by Ultrafast Laser Nanostructuring," *ACS Photonics* 4 (2017): 2944–2951, https://doi.org/10.1021/acsphotonics.7b01082.

48. S. Bertet, M. Mireles, S. MacNally, et al., "All-Alumina Quarter-Wave Plate Coatings Fabricated by Glancing Angle Deposition Using Serial Bideposition," *Applied Surface Science* 710 (2025): 163957, https://doi.org/10.1016/j.apsusc.2025.163957.

49. V. Ksianzou, R. K. Velagapudi, B. Grimm, and S. Schrader, "Polarization-Dependent Optical Characterization of Poly(Phenylquinoxaline) Thin Films," *Journal of Applied Physics* 100 (2006): 063106, https://doi.org/10.1063/1.2349471.

50. M. Ryu, M. Han, L. Grineviciute, et al., "RGB-Color Image Analysis for Determination of Birefringence of Micro-Films and Columnar Coatings," *Laser & Photonics Reviews* 17 (2023): 2200535.

51. Z. Tan, W. Guo, X. Fang, et al., "Dual-Substituent Poly(Vinyl Alcohol) With Tailored Wavelength Dispersion for Quarter-Wave Plates," *Polymer* 359 (2026): 130224, https://doi.org/10.1016/j.polymer.2026.130224.

52. P. Zhou, L. Ye, D. Yang, and J. Zhu, "Highly Enhanced Photoinduced Birefringence and Diffraction Efficiency of Methyl Orange/Polyvinyl Alcohol Composite Films for Polarization Holography by Controlling Ambient Humidity," *Optical Materials* 178 (2026): 118274, https://doi.org/10.1016/j.optmat.2026.118274.

53. X. Meng, Y. He, B. Dimitrov, et al., "Dynamic Mechanical Modulation of Chiroptical Structures via Linearly Assembled Plasmonic Nanoparticles on Birefringent Polymer Films," *Nature Communications* 16 (2025): 5156, https://doi.org/10.1038/s41467-025-60165-x.

54. G. Ghosh, "Dispersion-Equation Coefficients for the Refractive Index and Birefringence of Calcite and Quartz Crystals," *Optics Communication* 163 (1999): 95–102, https://doi.org/10.1016/S0030-4018(99)00091-7.

55. M. J. Dodge, "Refractive Properties of Magnesium Fluoride," *Applied Optics* 23 (1980): 1980–1985.

56. Z. Guoqing, X. Jun, C. Xingda, et al., "Growth and Spectrum of a Novel Birefringent α-BaB_2O_4 Crystal," *Journal of Crystal Growth* 191 (1998): 517–519.

57. H. T. Luo, T. Tkaczyk, E. L. Dereniak, K. Oka, and R. Sampson, "High Birefringence of the Yttrium Vanadate Crystal in the Middle Wavelength Infrared," *Optics Letters* 31 (2006): 616–618, https://doi.org/10.1364/OL.31.000616.

58. B. Song, H. Gu, S. Zhu, et al., "Broadband Optical Properties of Graphene and HOPG Investigated by Spectroscopic Mueller Matrix Ellipsometry," *Applied Surface Science* 439 (2018): 1079–1087, https://doi.org/10.1016/j.apsusc.2018.01.051.

59. H. Gu, X. Chen, H. Jiang, C. Zhang, and S. Liu, "Optimal Broadband Mueller Matrix Ellipsometer Using Multi-Waveplates With Flexibly Oriented Axes," *Journal of Optics* 18 (2016): 025702, https://doi.org/10.1088/2040-8978/18/2/025702.

60. A. Savin, R. Nesper, S. Wengert, and T. F. Fässler, "ELF: The Electron Localization Function," *Angewandte Chemie* 36 (1997): 1808–1832, https://doi.org/10.1002/anie.199718081.

Supporting Information

Additional supporting information can be found online in the Supporting Information section.

Supporting File: anie74532-sup-0001-SuppMat.docx.